Chemical Engineering Journal 489 (2024) 150956

Contents lists available at ScienceDirect

Chemical Engineering Journal

journal homepage: www.elsevier.com/locate/cej

An end-capping strategy for shape memory phthalonitrile resins via annealing enables conductivity and wave-absorption

Rongxiang Hu [a], Fenghua Zhang [a,*], Lan Luo [a], Linlin Wang [a], Yanju Liu [b], Jinsong Leng [a,*]

[a] Centre for Composite Materials and Structures, Harbin Institute of Technology (HIT), Harbin 150080, People's Republic of China
[b] Department of Astronautical Science and Mechanics, Harbin Institute of Technology (HIT), Harbin 150001, People's Republic of China

ARTICLE INFO

Keywords:
Shape memory polymer
Phthalonitrile resins
High thermal stability
Ablation resistance

ABSTRACT

Shape memory polymers (SMPs) with elevated switching temperatures and enduring thermal properties are highly desirable yet challenging in certain aerospace applications. In this study, high-temperature shape memory phthalonitrile resins (SMPNs) were developed using an end-capping strategy with the uniphthalonitrile (UPN) as the end-capping reagent to modulate the density of the cross-linked network. The resultant SMPNs exhibit a glass transition temperature (Tg) at approximately 300 °C, with a shape fixation rate of about 98 % and a shape recovery rate around 97 %. Importantly, these SMPNs also demonstrated exceptional thermal stability, with a thermal decomposition temperature exceeding 445 °C. Additionally, an oxyacetylene ablative test revealed the SMPNs' robust ablative resistance, as the linear ablation rate remained below 0.1 mm/s and the mass ablation rate was less than 0.1 g/s. The commendable shape memory performance and superior high-temperature resistance allowed the SMPNs to successfully undergo the shape recovery process when subjected to a butane flame. Furthermore, after a high-temperature annealing process, the SMPNs exhibited electrical conductivity due to graphitization, even possessing wave-absorbing properties within a specific frequency range. It is foreseeable that these multifunctional SMPNs will have extensive applications in the aerospace sector, given the advancement of smart structures.

1. Introduction

Shape memory polymers (SMPs) represent a category of intelligent materials capable of autonomous, programmable responses to external stimuli, including thermal, magnetic, electrical, and optical fields [1–3]. The distinctive attributes of SMPs, such as substantial deformability and low weight, have garnered significant attention in both academic and industrial circles, particularly in high-value engineering applications [4–8]. Thermal actuation remains the primary activation mode for SMPs, with the key determinant being the shape transition temperatures, either the melting temperature (T_m) or the glass transition temperature (T_g), dictating the range of applications. For example, shape memory polyurethane, featuring a T_g around 40 °C, has applications in smart textiles and biomedical materials [9,10], while shape memory epoxy ($T_g \sim 100$ °C) finds utility in space deployable structures [11,12]. Shape memory cyanate ester ($T_g \sim 200$ °C) is suitable for latch-release mechanisms in space environment actuators [13,14].

In the past decade, there has been widespread development of various SMP types, with extensive studies on their properties and applications [15–17]. However, only a limited number of SMPs exhibit trigger temperatures surpassing 300 °C, and even fewer can withstand harsh, ultra-high-temperature environments, which constrains their application in aerospace, machinery, and other demanding fields. Therefore, it is imperative to advance SMPs with higher trigger temperatures and enhanced thermostability.

Phthalonitrile (PN) resins represents a class of high-performance thermosetting resins known for their excellent attributes, originally developed by the U.S. Naval Research Laboratory in the early 1970s [18–20]. These resins possess numerous advantages, including high T_g (typically > 400 °C), exceptional thermal and thermal oxidation stability, flame resistance, and low water absorption. PN resins have been progressively applied in high-end domains like advanced composites, electronic packaging, adhesives, and carbon precursor materials [21–24]. While existing research primarily centers phthalonitrile monomer modification and corresponding resin properties [25–27], little is known about the shape memory characteristics of PN resins. Notably, bisphthalonitrile (BPN) resins are the dominant research focus among PN resins, with their excellent performance attributed to the

* Corresponding authors.
E-mail addresses: fhzhang_hit@163.com (F. Zhang), lengjs@hit.edu.cn (J. Leng).

https://doi.org/10.1016/j.cej.2024.150956
Received 8 January 2024; Received in revised form 10 March 2024; Accepted 1 April 2024
Available online 9 April 2024

abundant aromatic structures in the polymer network. Crosslinked heteroaromatic ring structures, such as triazine, polyisoindoline, and phthalocyanine, greatly improve the thermostability of PN resins [28,29]. However, the densely crosslinked networks provide remarkable thermostability while constraining polymer chain movement, which can lead to brittle fracture under high temperatures, limiting the applicability of high-performance PN resins [30].

This study employs an end-capping strategy to develop shape memory PN (SMPN) resins. Uniphthalonitrile (UPN) monomers, featuring a sole phthalonitrile group in the molecule, serve as end-capping reagents to modulate the crosslinked network densities of PN resins. The sole phthalonitrile group in UPN participates in crosslinking reactions with phthalonitrile groups to form heteroaromatic rings while avoiding the extension of the crosslinked network (Fig. 1a), allowing molecular chains to be released from crosslinked networks and facilitating polymer segment movement at high temperatures. As a result, the resulting SMPN resins exhibit a low modulus in rubber states, enabling them to reshape at temperatures surpassing T_g (~300 °C) with a shape fixation rate of approximately 98 %. To the best of our knowledge, this is the first report on shape memory research related to phthalonitrile resins. Additionally, the SMPN resins continue to demonstrate adequate thermal stability and exceptional ablative resistance, which bodes well for smart deformation in high-temperature environments. Surprisingly, SMPN resins maintain dimensional integrity during high-temperature annealing, transitioning from a soft state to a hard state. As the annealing temperature rises, the rigidified SMPN undergoes graphitization, becoming a conductor capable of absorbing electromagnetic waves within a specific frequency range. It is evident that high-temperature SMPN resins with multiple functionalities have significant application potential in the aerospace industry.

2. Material and methods

2.1. Materials and characterization

Bisphenol A, 4-nitrophthalonitrile, 4-phenylphenol, anhydrous potassium carbonate (K_2CO_3), dimethyl sulfoxide (DMSO), 4,4′-difluoro diphenylmethanone, phenol and bis[4-(3-aminophenoxy)phenyl] sulfone (m-BAPS) were obtained from Aladdin Reagent Co. (Shanghai, China), toluene were commercially available and used without further purification.

2.2. Synthesis of monomers

The synthesis routes of BPN and UPN are depicted in Fig. 1b and Fig. 1c. Two types of BPN monomers were synthesized, as previously reported [30]. The short-chain molecular BPN monomer based on bisphenol A was denoted as BPN-S, while the long-chain BPN monomer containing oligomeric multiple aromatic ether was labeled as BPN-L. Similarly, the end-capping reagent was synthesized using the same method, with the sole phthalonitrile group acting as the capping agent. The short-chain UPN monomer based on diphenyl was designated UPN-S, and the long-chain UPN monomer containing oligomeric multiple aromatic ether was labeled UPN-L. The specific synthetic procedures of UPN-S, BPN-S, UPN-L and BPN-L are given in the Supporting Information.

2.3. Preparation of the resins

The PN resins preformed polymer containing UPN and BPN was prepared by melting deaeration at 150 °C–200 °C with 5 wt% of the m-BAPS as curing additives. Once the curing additive had been evenly dispersed and degassed the compound for 10 min, the prepolymer was poured onto aluminum foil and cooled to room temperature. The

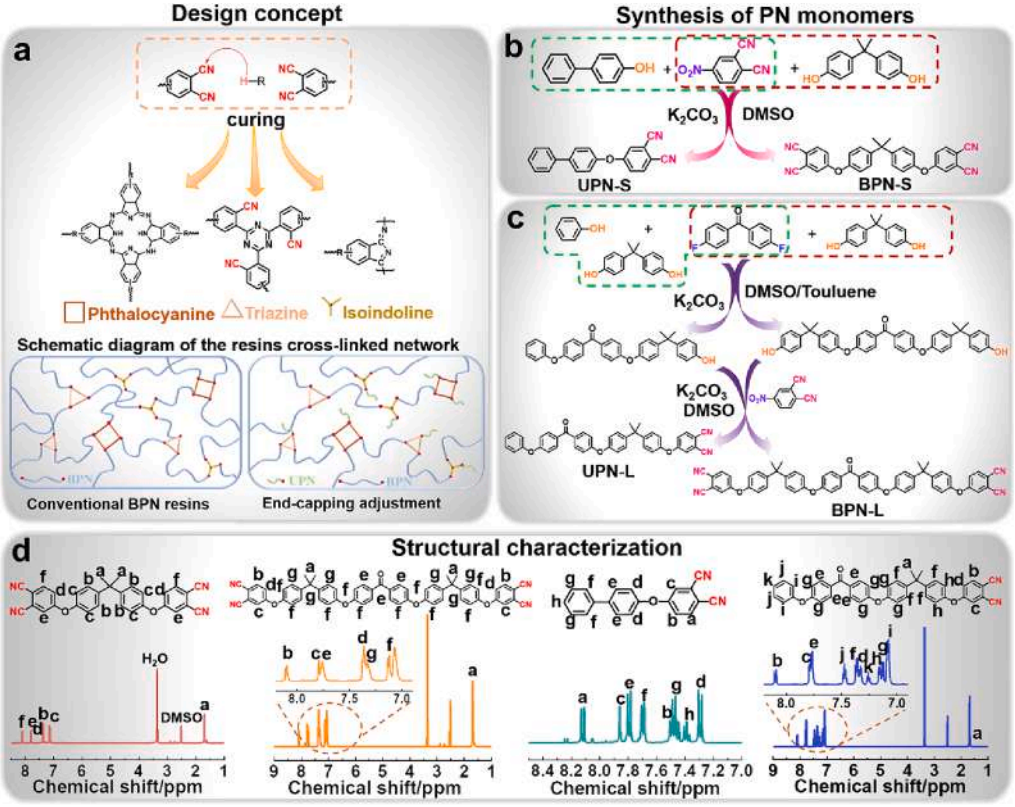

Fig. 1. (a) Design concept of the end-capping strategy of phthalonitrile resins. (b-c) Synthetic route of monomers. (d) ^{1}H NMR spectra of all the synthesized monomers.

components with different UPN and BPN monomers were marked as series labels, the label and corresponding component were given in Table 1.

The prepolymer was cured in the high-temperature oven under the following heating protocol: 220 °C for 2 h, 260 °C for 4 h, 280 °C for 4 h,300 °C for 4 h, 325 °C for 4 h, and 350 °C for 4 h.

2.4. Characterization

Fourier Transform infrared spectroscopy (FTIR) of all the synthesized monomers was investigated on a Nicolet-Nexus-670 FT-IR spectrometer from 4000 cm^{-1} to 400 cm^{-1} using the KBr disk method. The structure of the monomers was characterized by nuclear magnetic resonance (NMR) (400 MHz, DMSO). Differential scanning calorimetry (DSC) analyses of the monomers and prepolymers were performed on Mettler-Toledo TGA/DSC STARe System scanned from 25 °C to 350 °C at a heating rate of 10 °C /min in the nitrogen atmosphere. Thermogravimetric analysis (TGA) was heated from 25 °C to 1000 °C at a heating rate of 10 °C /min in the nitrogen atmosphere. Dynamic rheological analysis (DRA, AR-G2, TA Instrument) was used to study the processability and curing reaction of the prepolymers. Dynamic mechanical analysis (DMA) was performed to investigate the dynamic mechanical properties of obtained resins using the DMA Q800 (TA Co., America) recorded in multi-frequency strain mode at a constant frequency of 1 Hz with a heating rate of 5 °C min^{-1} from 25 °C to 480 °C. The oxyacetylene flame ablation test was performed with an oxygen flow of 1420 L/s and acetylene flow of 1200 L/s to research the oxidation ablative properties of SMPN with cylindrical-shaped specimens of 10 mm thickness and 30 mm diameter. A scanning electron microscope (SEM) was used to observe the microscopic morphology of the Hitachi SU3900. The Raman spectra were recorded by the Laser confocal Raman Spectrometer (Thermo Scientific DXR2xi) with laser lines of 455 nm. The coaxial line method was used to obtain the electromagnetic parameters by Vector Network Analyzers (Agilent E5071C) in the frequency range of 1–18 GHz, and the microwave absorption performance was calculated according to transmission line theory as in the following equation:

$$Z_{in} = Z_0\sqrt{\frac{\mu_r}{\varepsilon_r}}\tanh\left(j\left(\frac{2\pi fd}{c}\right)\sqrt{\mu_r\varepsilon_r}\right) \quad (1)$$

$$RL(dB) = 20\lg\left|\frac{Z_{in}-Z_0}{Z_{in}+Z_0}\right| \quad (2)$$

Table 1
Component of the defined samples.

Sample label	the molar ratio of BPN and UPN
A-0	BPN-S/1 mol: UPN-S/0 mol
A-0.5	BPN-S/1 mol: UPN-S/0.5 mol
A-1	BPN-S/1 mol: UPN-S/1 mol
A-1.5	BPN-S/1 mol: UPN-S/1.5 mol
A-2	BPN-S/1 mol: UPN-S/2 mol
B-0	BPN-S/1 mol: UPN-L/0 mol
B-0.5	BPN-S/1 mol: UPN-L/0.5 mol
B-1	BPN-S/1 mol: UPNB-L/1 mol
B-1.5	BPN-S/1 mol: UPN-L/1.5 mol
B-2	BPN-S/1 mol: UPN-L/2 mol
C-0	BPN-L /1 mol: UPN-S/0 mol
C-0.5	BPN-L /1 mol: UPN-S/0.5 mol
C-1	BPN-L /1 mol: UPN-S/1 mol
C-1.5	BPN-L/1 mol: UPN-S/1.5 mol
C-2	BPN-L/1 mol: UPN-S/2 mol
D-0	BPN-L/1 mol: UPN-L/0 mol
D-0.5	BPN-L/1 mol: UPN-L/0.5 mol
D-1	BPN-L/1 mol: UPN-L/1 mol
D-1.5	BPN-L/1 mol: UPN-L/1.5 mol
D-2	BPN-L/1 mol: UPN-L/2 mol

3. Results and discussion

3.1. Characterization of the monomers

The structures of all synthesized monomers were verified through Fourier Transform infrared spectroscopy (FTIR) and proton nuclear magnetic resonance (^{1}H NMR) techniques. FTIR spectra of all the synthesized monomers are presented in Fig. S1. The FTIR curves of all the obtained monomers show that the typical characteristic absorption peak of the cyano group (C≡N) and aromatic oxide group (Ar—O—Ar) were absorbed at around 2230 cm^{-1} and 1250 cm^{-1}, respectively, which means the end-capping of phthalonitrile group. ^{1}H NMR spectra, as shown in Fig. 1d, further validate the molecular structures, with absorbed peaks corresponding precisely to the synthesized monomers. The structure identified details of UPN-S, BPN-S, UPN-L and BPN-L were given in Supporting Information.

Differential scanning calorimetry (DSC), an efficient method for exploring material thermal transitions, was employed to study the thermal behavior of the monomers and their corresponding prepolymers (containing 5 wt% curing agent of m-BAPS). Fig. S2 shows that all the synthesized monomers present only one melting or softening endothermic peak with no additional thermal transition behaviors, signifying the purity of the monomers. Upon the addition of a curing agent, the prepolymers exhibit a curing exothermic peak at around 250 °C, and the curing exothermic peak of the UPN-L increase to around 270 °C. The higher curing reaction temperature of the UPN-L prepolymer is attributed to the longer molecular segment of the monomer and the lower density within the UPN-L system, reducing the interaction opportunities of the phthalonitrile group and increasing the activation energy of the curing reaction.

3.2. Processability of blended phthalonitrile prepolymers

Prepolymers were prepared by melt blending of UPN and BPN with a 5 wt% curing agent. The prepolymers with varying UPN and BPN compositions were labeled as series A, B, C and D, with specific compositions detailed in the experimental section. DSC was used to further investigate the curing behavior of the blended prepolymers. Fig. 2a demonstrates that the melting temperature of UPN-S and BPN-S blended prepolymers (A series) gradually decreased (from 192 °C down to 153 °C) as the UPN-S content increased. The presence of UPN-S disrupted the ordered arrangement of BPN-S molecular, resulting in a reduced melting point. All A-series blended prepolymer exhibited a single exothermic peak at approximately 246 °C, suggesting that all phthalonitrile groups within the blended prepolymer required similar energy for curing. However, the presence of UPN-S diluted the density of phthalonitrile groups, increasing the activation energy of the curing reaction and rising the exothermic peak temperature. Similar trends were observed in the B series, C series and D series blended prepolymer (Fig. 2b–2d), indicating a common thermal transition trend for UPN blended into the BPN system. The longer molecular segment of UPN-L led to a lower density of phthalonitrile groups in the corresponding blended prepolymers, causing a higher curing temperature. The oligomeric multiple aromatic ether segment of BPN-L also reduced the interaction opportunities of phthalonitrile groups compared to the BPN-S system, increasing the energy required for curing. Additionally, the melting or softening temperature of all the blended prepolymers decreased to varying degrees upon UPN blending, facilitating the processing of PN resins.

Rheological properties of prepolymers provide insight into their processability. The processing temperature window of PN resins refers to the temperature range where the prepolymer possesses sufficiently low viscosity for impregnation, a vital factor for industrial applications. Viscosity-temperature curves of A-series blended prepolymers are shown in Fig. 2e. The processing temperature window of A-0 (BPN-S prepolymer) was approximately 70 °C, melting at around 190 °C and

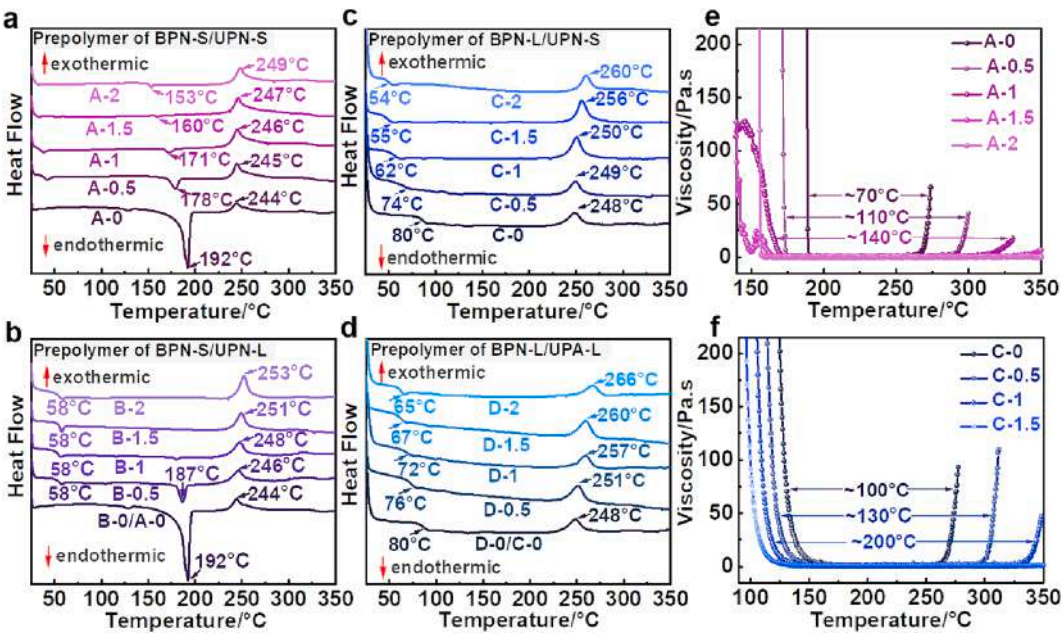

Fig. 2. (a-d) DSC curves of the series blended prepolymers. Viscosity-temperature curves of the blended prepolymer of (e) UPN-S/BPN-S and (f) UPN-S/BPN-L.

gelling at about 260 °C. As the UPN-S content increased, the melting temperature of the blended prepolymer decreased from 190 °C to about 155 °C, consistent with the DSC results. Fig. 2a and Fig. 2c show that the blending UPN-S had a limited effect on the curing exothermic temperature. However, the gelation temperature (T_{gel}) of A-series blended prepolymers increased significantly with increasing UPN-S content. For A-0, T_{gel} was approximately 260 °C with a heating rate of 5 °C /min. In contrast, A-0.5, A-1, and A-1.5 exhibited T_{gel} values of approximately 280 °C, 320 °C and 350 °C, respectively, obviously delaying gelation. This increase in T_{gel} was attributed to the end-capping effect of UPN-S, which inhibited the extension of polymeric networks and delayed the viscosity increase of the prepolymers. When the BPN-S to UPN-S molar ratio was approximately 1:10.5, A-1.5 exhibited no significant gelation even as the temperature reached 350 °C with a heating rate of 5 °C /min. This can be explained by the abundant end-capping reagents of UPN-S dramatically restraining the elongation of the crosslinked networks.

With the UPN-L working as end-capping reagent, the rheological properties of B-series prepolymers followed a similar trend. Fig. S3a shows that the viscosity of B-0.5 increased and decreased before the prepolymer completely flowed, which was due to the long-chain UPN-L having a lower softening temperature, allowing it to facilitate the rearrangement of BPN-S molecules at elevated temperatures. The full flow state temperature range for B-0.5 was around 130 °C, indicating a wide processing window. However, with increasing UPN-L content, the viscosity of B-1 prepolymer barely increased until 350 °C with a heating rate of 5 °C /min. The long-chain UPN-L reduced the density of phthalonitrile groups and further weakened the crosslinking reaction rate. In the BPN-L system, the blending of UPN-S or UPN-L similarly expanded the temperature range with low viscosity (Fig. 2f and Fig. S3b), widening the processing window. When the molar ratio of UPN-S or UPN-L to BPN-L exceeded 1:1, the processing temperature window extended 200 °C. Thus, the end-capping reagent of UPN effectively lowered the melting temperature of the prepolymer and delayed gelation, facilitating the resin processing.

The cross-linking density of the resins obtained through the end-capping strategy was indirectly evaluated by the gel content, which was tested by Soxhlet extraction according to the ASTM D2765 method [31]. The experimental details and the test results of the gel content were given in Supporting Information. Fig. S4 shows that the gel content of all the resins is maintained at a high level, which can be attributed to the formation of abundant heteroaromatic ring structures. However, the gel content of the resin is reduced slightly with the increase of end-capping reagent, which means the decrease of cross-linking density, demonstrating that the crosslinking network of the resin can be modulated by the end-capping strategy.

3.3. Thermomechanical behavior

After a temperature-programmed curing process, the PN resins are obtained. To assess the structure of the co-cured polymer, the FTIR analysis of A-series resins was conducted on behalf of the end-capping adjusted resins. Fig. S5 displays the normalized FTIR spectra of A-series resins with different curing process. After the curing reaction, the stretching vibration peak of − CN at 2230 cm^{-1} significantly weakened, and new peaks appeared at around 1355 cm^{-1} and 1519 cm^{-1}, indicating the formation of triazine. The peak at 1713 cm^{-1} suggests the presence of isoindoline, while the weak absorption peak at approximately 1013 cm^{-1} pertains to the skeletal vibration of phthalocyanine [32,33]. The absorption peak of the cyano groups around 2230 cm^{-1} did not disappear completely due to the retention of partial cyano groups within the triazine structure formed by phthalonitrile groups.

The thermomechanical behavior of the obtained polymers was characterized using dynamic mechanical analysis (DMA). Different curing processes yield resins with varying thermomechanical behaviors. Fig. S6 presents the DMA curves of A-series resins under different maximum curing temperatures. Although the resins cured at a maximum temperature of 325 °C exhibit a low modulus in the rubber state (Fig. S6a), which facilitates deformation, the FTIR analysis (Fig. S5a) indicates that some residual phthalonitrile groups remained unreacted. The TGA curves (Fig. S7a) also suggest the poor thermostability of these resins. Increasing the curing temperature allowed the phthalonitrile groups to react further (Fig. S5b), resulting in significantly improved thermostability for these resins (Fig. S7b). When the curing temperature reached 375 °C, the resins exhibited a higher T_g (Fig. S6c). However, while the higher curing temperature led to a higher T_g, it also resulted in a high modulus in the rubber state. Even at 415 °C (T_g + 40 °C), the modulus of A-2 still exceeded 400 MPa, making it challenging to deform due to its stiffness. The resins cured at a maximum temperature of 350 °C demonstrated decent stiffness variation (Fig. S6b) and thermostability (Fig. S7b), with a relatively complete curing reaction of phthalonitrile

groups. Therefore, the studied resins were subjected to a curing procedure of 220 °C/4h, 260 °C/4h, 280 °C/4h, 300 °C/4h, 325 °C/4h, and 350 °C/4h.

The DMA curves of the series resins are displayed in Fig. 3a–3d, and Table 2 provides the modulus of the studied resins in the glass state ($E_{25^\circ C}$), intermediate state ($E_{Tg-40^\circ C}$), and rubber state ($E_{Tg+40^\circ C}$). Overall, the T_g of the resins gradually decreased, and the storage modulus in the rubber state also decreased as the UPN content increased. This reduction in crosslinked network density, resulting from the end-capping effect of UPN, weakened the bonds of polymeric networks and facilitated the movement of polymer segments. Comparing Fig. 3a and Fig. 3b, the resins containing UPN-L exhibited a relatively lower storage modulus in the rubber state than the resins containing UPN-S at a similar molar ratio, especially when the blending molar ratio of UPN and BPN exceeded 1:1. This can be explained by the UPN-L containing an oligomeric multiple aromatic ether segment, which facilitated the movement of polymeric segments and resulted in a similar tendency as shown in Fig. 3c and Fig. 3d. A comparison between Fig. 3a and Fig. 3c revealed that the resins based on BPN-L exhibited a lower storage modulus in the rubber state than the resins based on BPN-S blended with an equal molar ratio of UPN-S. The abundance of the soft aromatic oxide segment in BPN-L made the polymer skeleton more flexible. When UPN-L, as the end-capping reagent, was co-cured with BPN-L, the DMA curves (Fig. 3d) indicated that the flexible segment reduced the modulus in the rubber state compared to those resins with an equivalent molar ratio of UPN and BPN. The DMA analysis of the series resins suggested that the stiffness of the resins in the rubber state significantly decreased with increasing UPN content, and the flexible aromatic oxide segment in the polymer skeleton favored the movement of the molecular network, making it easier for the resins to deform at high temperatures.

The flexibility properties of the investigated resins were assessed using a three-point bending test. Fig. 3e demonstrates that the bending strength of BPN-S-based series resins exhibited a trend of initial increase and subsequent decrease with increasing end-capping reagent content, whether it was end-capped with UPN-S or UPN-L. Resins with approximately half of the molar content of the end-capping reagent had higher flexibility than the BPN-S resin. This was due to the decreased crosslinked network density, which provided the polymer segment with more free space for movement, resulting in improved bending properties. However, with a continuous increase in UPN content, the bending strength of the resins decreased, as an excess of the end-capping reagent ceased the extension of polymeric chains, reducing the length of the polymer chains and weakening the interaction of segments. A similar trend was observed in the BPN-L-based series resins (Fig. 3f). Resins containing UPN-L exhibited better bending properties than those containing UPN-S with the same content, attributed to the longer molecular segment of UPN-L enhancing the entanglement of polymeric chains and improving flexural strength. Fig. S8 also provides the flexural modulus of the studied series resins. The resins with approximately 50 % molar proportion of the end-capping reagent demonstrated optimal flexural properties, and the polymer skeleton, which contained a flexible aromatic oxide segment, improved the flexural properties of the co-cured resins.

Table 2
The T_g, storage modulus before and after T_g of the Cured Phthalonitrile Resins.

Sample	$E_{25^\circ C}$/MPa	T_g/ °C	$E_{Tg-40^\circ C}$/MPa	$E_{Tg+40^\circ C}$/MPa
A-0	3571	436	1014	359
A-0.5	3851	364	1123	298
A-1	3835	355	1187	194
A-1.5	3707	322	1031	170
A-2	3647	306	1158	120
B-0.5	3371	353	1063	227
B-1	2860	328	1106	124
B-1.5	3246	276	1017	71
B-2	3019	253	1082	35
C-0	2884	380	939	238
C-0.5	3380	328	1082	184
C-1	3189	308	949	89
C-1.5	3537	290	941	76
C-2	3170	275	865	48
D-0.5	2719	330	932	146
D-1	2531	318	967	81
D-1.5	2665	292	1122	47
D-2	2610	264	1483	23

3.4. Shape memory function

The shape memory performance of the obtained resins was evaluated using the bending deformation method. Specific test details are available in the Supporting Information and Fig. S9. Table S1 and S2 provide the specific shape fixity ratio (R_f) and shape recovery ratio (R_r) for each resin. Resins with relatively high storage modulus in the rubber state cannot be deformed above the glass transition temperature (T_g), such as A-0, A-0.5, B-0.5, and so on, making it difficult to determine R_f and R_r. By adjusting the crosslinked network density with an end-capping reagent, resins with softer stiffness in the rubber state exhibited excellent shape memory performance, with R_f exceeding 98 % and R_r around 97

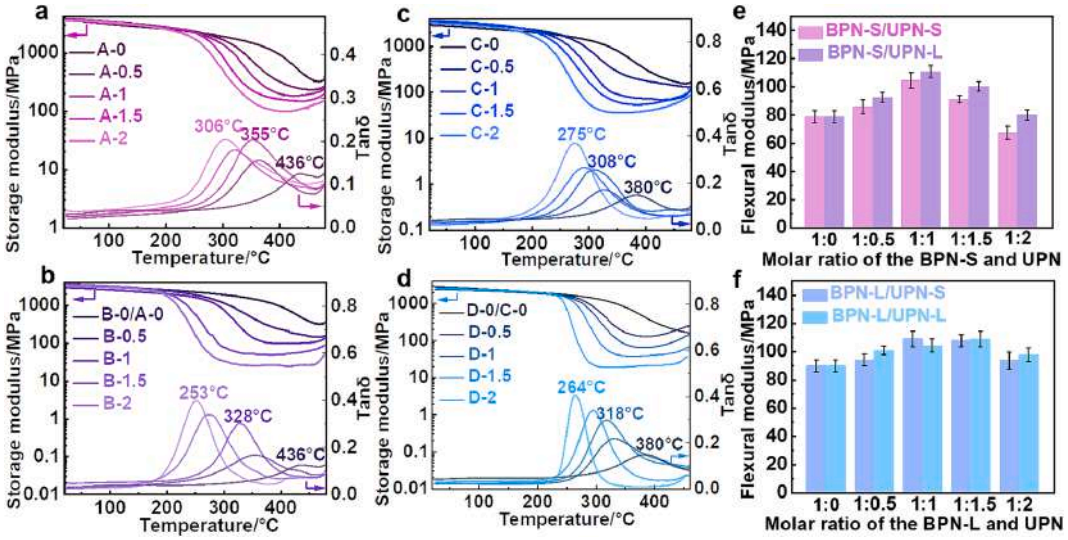

Fig. 3. (a-d) DMA curves of the series co-cured resins. (e-f) The bending strength of the series co-cured resins.

%. The end-capping of UPN, reduced the connections between crosslinked networks in the phthalonitrile resin, facilitating polymer segment movement at high temperatures and enabling resin deformation, and leading to the acquisition of shape memory properties. Fig. S9b provides images of the original shape, temporary shape, and recovery shape of the D-1. In addition, the two-cycle shape memory performance of the D-1 sample was tested by DMA in three-point bending mode; the recorded temperature, force, and displacement over time are shown in Fig. S10. The shape fixity rate of the first and second cycles were determined to be greater than 97 %. The shape recovery rate is lower than the tested results of bending deformation method with 87 % in the first cycle and 90 % in the second cycle, which can be attributed to insufficient recovery time and the differences in test methods. According to the shape memory mechanism of SMPs, in shape memory phthalonitrile (SMPN) resins, crosslinking structures like triazine, polyisoindoline, and phthalocyanine serve as the fixed phase, determining the permanent shape of the resin, while the aromatic oxide polymeric chains act as the reversible phase, playing an important role in fixing temporary shapes [7]. When the SMPN is deformed under the action of external forces in the rubber state, the relative position of the fixed phase is well preserved, while the molecular chains of the reversible phase rearranged undergo the direction of the force. Once the SMPN has cooled, the reversible phase transformed from the rubbery state to the glassy state with the elastic potential energy of molecular chains stored, and the temporary shape is fixed. When the SMPN is reheated and returns to its rubber state, the energy stored in the reversible phase is released and the resin recovers to its initial shape with the help of the fixed phase.

To evaluate the applicability of SMPN, D-1, which exhibits good shape memory performance and thermostability, was processed into various structures and deformed into temporary shapes. Fig. 4a illustrates a potential application scenario for SMPN in variant aircraft. The flat SMPN-based airfoil was deformed into a warping temporary shape at 330 °C and then fixed as the temperature dropped to ambient temperature. A heat gun simulated pneumatic friction as a thermal source. When the aircraft flew at high speed and generated pneumatic friction at high temperatures, the SMPN-based warping airfoil could actively deform to adjust its flight attitude. As shown in Fig. 4a and Supporting Video 1, the SMPN-based airfoil completed the deformation process within 25 s, responding quickly to the high temperature (the heat gun temperature was set at 350 °C). Fig. 4b demonstrates the transformation process of the SMPN-based stellate sample, recovering from a gathered temporary shape to its unfolded initial shape when heated in an oven. The temporary transformed shape was recorded every 30 s, with the sample removed from the high-temperature oven at 330 °C.

3.5. Thermal stability

The thermal stability of the prepared resins was assessed via Thermal Gravimetric Analyzer (TGA) from room temperature to 1000 °C in a nitrogen atmosphere (Fig. 4a–4d). The temperatures at which a 5 % weight loss ($T_{5\%}$) occured for all the studied resins exceeded 445 °C, and the carbon residue yield at 1000 °C (C_{y1000}) for these resins was no less than 60 %, indicating excellent thermal stability. Among all the resins, those cured without an end-capping reagent displayed the highest thermal stability. The thermal stability of the BPNB-based series resin was lower than that of the BPN-S-based series resin, which was co-cured with the same end-capping reagent. This difference can be attributed to the crosslinked network of BPN-L, which is less dense due to its longer aromatic oxide segment, allowing thermal-decomposed molecules easier to escape more easily from the polymeric network. With the end-capping of UPN, the polymer network of the resins loosened further, and the resins containing UPN-S (Fig. 5a and 5c) exhibited better thermal stability than those containing UPN-L (Fig. 5b and 5d) in the same BPN-based resins. Although the thermal stability of the resins end-capped by UPN decreased to some extent, the abundant aromatic structures in the polymer still provided the resins with decent high-temperature resistance.

It has been reported that the PN resins treated at high temperatures in an oxygen-free atmosphere can maintain the dimensional integrity of the sample with some shrinkage. They even exhibit conductivity at temperatures above 600 °C [34]. In this study, to investigate the variations in structure and properties of thermally treated phthalonitrile resins, D-1 was annealed at 500 °C, 600 °C, 700 °C and 800 °C for 1 h under nitrogen. These samples were marked as A500, A600, A700, and A800, respectively. X-ray diffraction (XRD) was used to examine the crystalline structure of the annealed specimens. Fig. 5e shows that the D-1 sample exhibited a broad diffraction peak at around $2\theta = 17.5^{\circ}$, which corresponds to the amorphous structure of the resin. When annealed at 500 °C, the peak around $2\theta = 17.5^{\circ}$ became broader, and the peak shifted slightly to a higher angle. This indicates limited structural changes with the 500 °C thermal treatment. As the annealing temperature rose to 600 °C, the broad peak of the original resins almost entirely shifted to around $2\theta = 25^{\circ}$, which refers to the (0 0 2) crystallographic planes of hexagonal graphite-like carbon. With increasing annealing temperature, the diffraction peaks of (0 0 2) crystallographic planes became more pronounced, and (1 0 0) crystallographic planes at around $2\theta = 44^{\circ}$ also appeared, indicating the formation of graphite-like structures.

Raman spectra were employed to confirm the existence of graphite-like structures in the annealed D-1 resins. Fig. 5f shows two distinct bands at 1344 cm^{-1} (D-band) and 1592 cm^{-1} (G-band) in the annealed

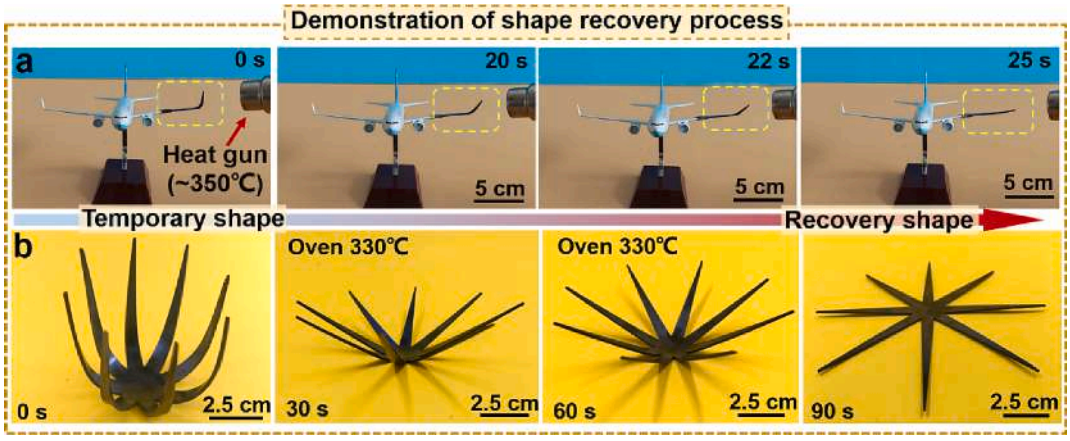

Fig. 4. (a) Digital photos of the shape recovery process of SMPN with a warping shape. (b) The shape recovery process of the object with gathered temporary shape under the heating of an oven.

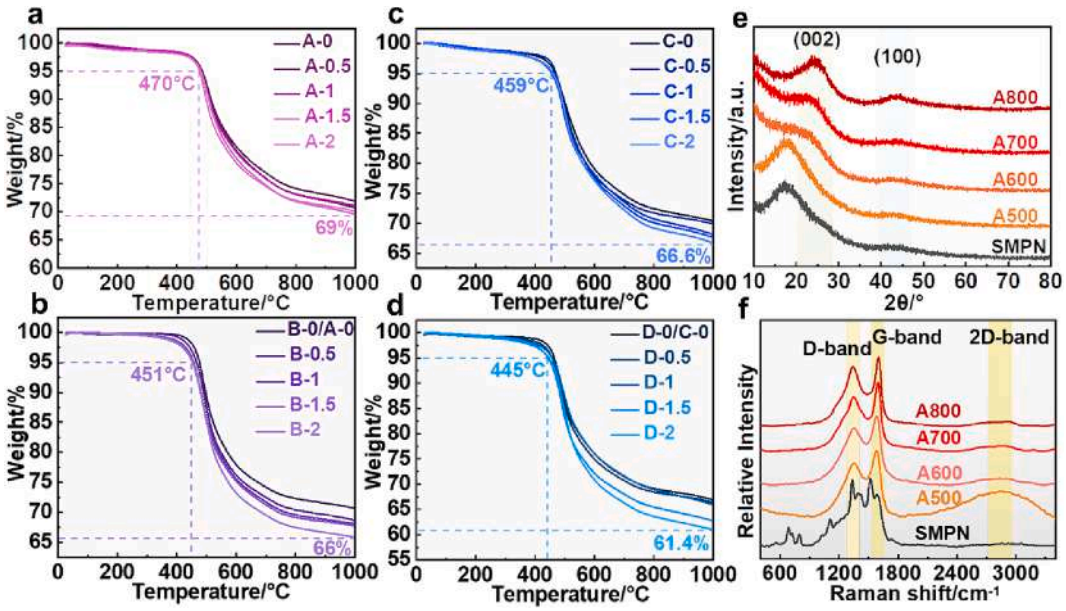

Fig. 5. (a-d) TGA curves of the series co-cured resins. (e) XRD curves and (f) Raman spectra of heat-treated D-1 at different annealing temperature.

SMPN. The emergence of the 2D-band at around 2800 cm^{-1} after annealing at 500 °C became less prominent as the annealing temperature increased. The D-band represents the disorder or defect in the graphitic carbon structure, while the G-band represents the planar configuration of sp^2 bonded carbon in graphene and graphite [35,36]. The increasing sharpness of the G-band indicates the graphitization of the aromatic backbone, making the π orbitals easier to overlap at higher temperatures. The stronger D-band may result from the graphitization of the sidechain after thermal decomposition, increasing the quantity of graphite-like microcrystals and the carbon atoms at the edges of these microcrystals as the annealing temperature rises.

Equipped with the shape memory property and excellent thermal stability, SMPN provides a promise for applications in extremely high-temperature environments. The butane flame, with flame temperatures up to 1000 °C, was used as a high-temperature heating source to stimulate the SMPN [37]. Fig. 6a and Supporting Video 2 show that the gathered temporary shape of the stellate sample could recover to the unfolded initial shape within 15 s, and no burning occurred during the recovery process. This demonstrates the potential of SMPN in applications in extremely high-temperature environments. Fig. S11 displays the SMPN-based conical thermal protection shell and its corresponding temporary shape, while Fig. 6b shows the recovery process of the conical shell. When exposed to a butane flame heat source, the shell gradually recovers its original conical shape. The excellent shape memory performance and good temperature resistance make SMPN suitable for applications in smart deformation and heat protection fields. Although SMPN could recover the shape quickly in extremely high-temperature environments, the thermal damage of the SMPN matrix is irreversible for the thermal decomposition. The shape memory effect can hardly be operated repeatably in the environment above thermal decomposition temperature.

3.6. Ablation resistance performance

The thermal stability of the SMPN resins is comparable to traditional ablative resins such as phenolic resin and benzoxazine resin, and it is reported that phthalonitrile resins also have decent ablation resistance [37–39]. Therefore, an oxyacetylene flame was used to evaluate the ablation resistance performance of SMPN. The D-1 resin was processed into a cylinder and secured by a high-temperature-resistant fixture (Fig. 7a). The sample was subjected to the ultrahigh-temperature flame, exceeding 2000 °C, for 20 s, 30 s, and 50 s. The temperature on the

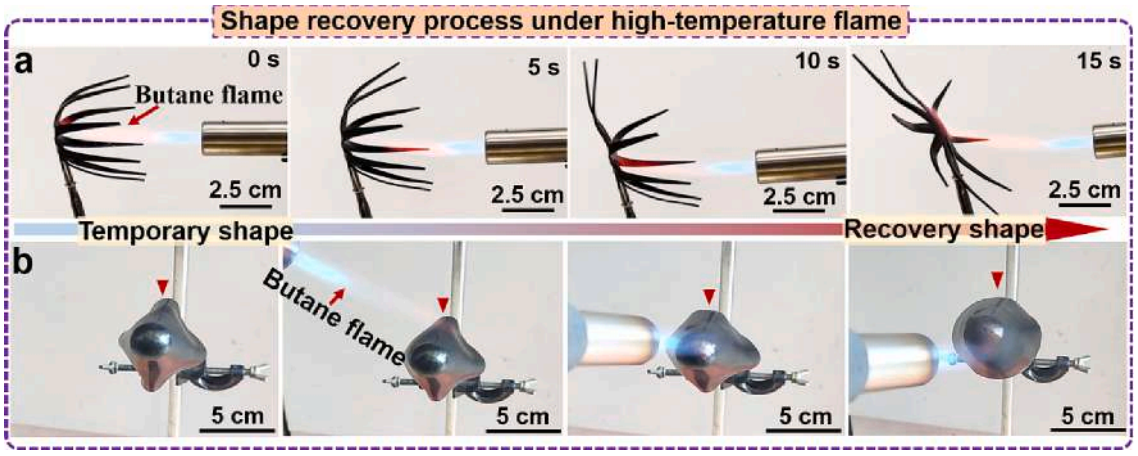

Fig. 6. (a) The shape recovery process of the object with gathered temporary shape under the heating of a butane flame. (b) The shape recovery process of the conical thermal protection shell under the heating of a butane flame.

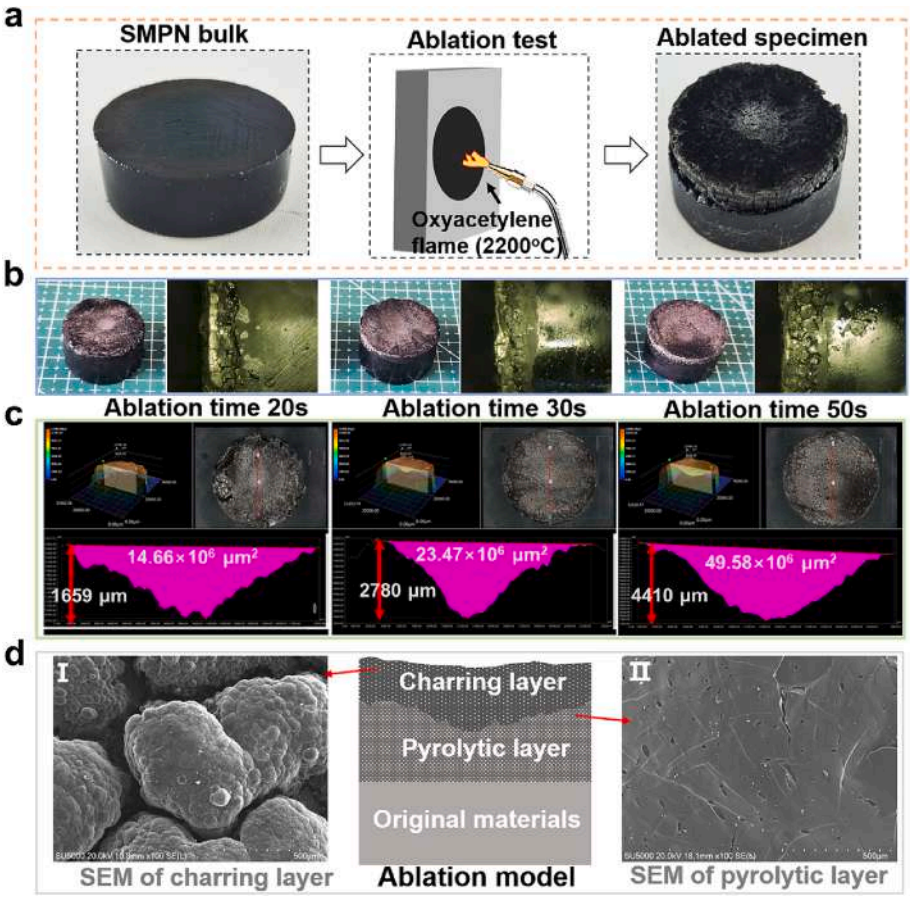

Fig. 7. (a) Sample photograph and the test schematic configuration of oxyacetylene flame. (b) Digital photos and (c) 3D digital microscope images of the ablative specimen with different ablation times. (d) Ablation model and SEM images of the ablated specimen.

sample surface was recorded and is shown in Fig. S12. Fig. 7b displays digital photos of the ablative specimen at different ablation times. Side photos of the ablative specimen reveal the appearance of an oily-like liquid oozing from the ablating layer as the ablation time increased. This liquid is likely composed of ultrahigh-temperature decomposition products of the resin. Frontal surface images (Fig. S13) of the ablative specimen show abundant cracks, resulting from the ultrahigh-temperature flame.

The ablation mechanism of polymer-based ablative materials typically involves three components within the matrix during ablation: the charring layer, pyrolytic layer, and original materials [40,41]. SEM was employed to examine the microscopic morphology of the specimen with a 30-s ablation time. Fig. 7d illustrates the ablation model of the ablative polymer, with Fig. 7dI showing the charring layer of SMPN displaying cracked bulk particles with numerous small bulges. These cracked bulk particles are likely due to thermal expansion of the specimen in an ultrahigh-temperature environment. Simultaneously, the resin on the surface cracks and carbonizes. Examining the interior of the ablative specimen, the SEM image (Fig. 7dII) reveals numerous holes in the pyrolytic layer, caused by the escape of pyrolysis gases at high temperatures. As the pyrolysis gases permeate the surface, they absorb and block energy passing through the char, and some of the energy is released as the pyrolysis gases escape from the charring layer.

The oxyacetylene flame ablation properties of the specimen with different ablation times are listed in Table 3. The linear ablation rate (LAR) of the specimens with ablation times of 20 s, 30 s, and 50 s were 0.08295 mm/s, 0.09267 mm/s, and 0.0882 mm/s respectively, and the corresponding mass ablation rate (MAR) was 0.08289 g/s, 0.07389 g/s and 0.06527 g/s. MAR decreased slowing as the ablation time was extended, which can be attributed to the formation of a charring layer that prevented the invasion of ultrahigh-temperature heat and slowed down the speed of thermal decomposition. Fig. 7c shows the observation results of the 3D Digital Microscope, indicating that the center of the specimen, which mostly withstood the ultrahigh-temperature flame mostly, was severely ablated. However, the LAR remained at low levels and relatively stable as the ablation time extended. The ablation test results demonstrate that SMPN possesses excellent ablation resistance, making it highly promising for high-temperature deformation applications with ablation resistance.

Table 3
Ablation properties of the specimen with different ablation times.

Specimen	LAR (mm/s)	MAR (g/s)
D-1/20 s	0.08295	0.08289
D-1/30 s	0.09267	0.07389
D-1/50 s	0.0882	0.06527

3.7. Wave-absorbing function

The obtained SMPNs have a high T_g at around 300 °C, and their high carbon residue yield indicates excellent high-temperature resistance, which shows SMPN an extensive high-temperature applications. Compared to previous studied SMPs [17,42–50], the developed SMPNs should be among the top materials in terms of their ability to withstand higher temperatures (Fig. 8a). Furthermore, when SMPN is exposed to an environment exceeding its decomposition temperature, it maintains its structural integrity and becomes rigid during decomposition. Fig. 8b displays DMA curves of the D-1 resin treated at 500 °C for 60 min under

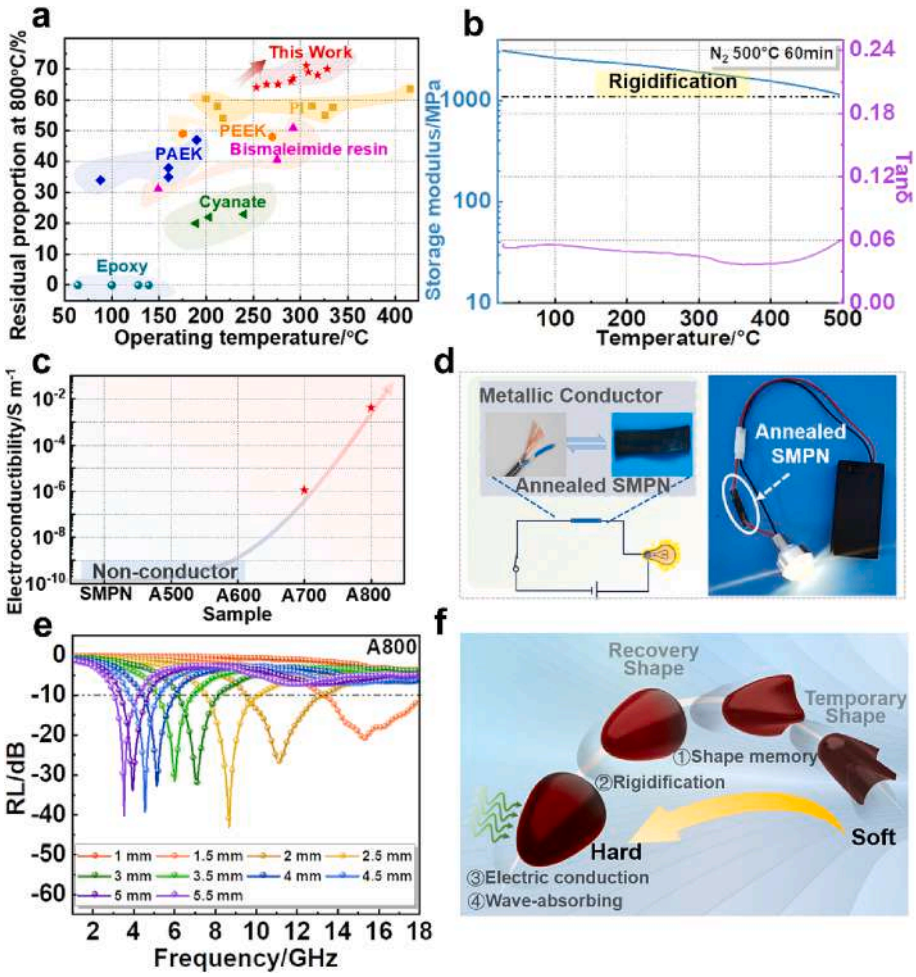

Fig. 8. (a) Relationship between SMPN and previous SMPs. (b) DMA curves of D-1 after annealing at 500 °C for 60 min in a nitrogen atmosphere. (c) The variation curve of conductivities during the annealing process. (d) Conductivity in annealed SMPN. (e) Frequency-dependent reflection losses of A800. (f) Illustrative diagram of an SMPN-based thermal protection shell.

a nitrogen atmosphere. After annealing, no glass transition process is observed within the tested temperature range, and the storage modulus of the resin remains around 1000 MPa even at temperatures around 500 °C, indicating the rigidification of SMPN. As the annealing temperature increases, the graphitization process (Fig. 5e and 5f) of SMPN enhances, endowing the resin with conductivity. The conductivity of annealed SMPN is provided in Table S3, and the relationship between conductivity and the annealing process is shown in Fig. 8c. Resins treated below 600 °C are non-conductive as conductivity cannot be measured using the four-probe tester. However, the resin annealed at 700 °C exhibits a conductivity of 1.12×10^{-6} S m^{-1}, and the conductivity increases to 4.21×10^{-3} S m^{-1} when the annealing temperature reaches 800 °C. Fig. 8d demonstrates that the annealed SMPN (A800) can function as a conductor to carry current and power a light bulb.

Surprisingly, the annealed SMPN also has the capacity to absorb electromagnetic waves. The electromagnetic properties of annealed SMPN were evaluated using Vector Network Analyzers in the frequency range of 1–18 GHz, and Fig. S14 shows the electromagnetic parameter curves versus frequency. It is known that the real part permittivity (ε') of the complex dielectric constant represents the storage ability of electric energy, while the imaginary part permittivity (ε") represents the dissipation capacity of electric energy [51]. Fig. S14 shows that in the examine range of 1–18 GHZ, the real part permittivity of the dielectric constant of A800 monotonically decreases and the imaginary part permittivity monotonically increases with increasing frequency. There is no significant relaxation behavior of polarization, which may be attributed to the conduction loss dominating the absorption of electromagnetic waves. The wave-absorbing performance of A800 was calculated according to transmission line theory, and Fig. 8e presents the calculated reflection loss curves. When the reflection loss (RL) values are below − 10 dB, it indicates that over 90 % of the microwave is absorbed and attenuated [52]. The RL curves of A800 reveal that the annealed SMPN exhibits strong wave-absorbing performance at specific frequencies. As the annealed resin A800 is a conductor with a conductivity of 4.21×10^{-3} S m^{-1}, the electromagnetic loss mechanism was interpreted from a conduction loss perspective [53]. As annealing temperature increases, the increased conductivity brings a greater macroscopic current caused by the carrier, which is conducive to the conversion of electromagnetic energy into heat energy, resulting in the absorption and attenuation of microwave.

Integrating the properties of shape memory, high-temperature resistance, rigidification, and microwave absorption, SMPN can be used in more complex application scenarios. Fig. 8f illustrates the potential application of an SMPN-based thermal protection shell: it can undergo a shape recovery process during high-speed flight, become rigid from a soft state to a hard state under high temperatures, and absorb electromagnetic waves due to graphitization. It is foreseen that the developed SMPNs would promote the further applications of SMP in the field of high-temperature smart deformation.

4. Conclusion

In summary, multifunctional SMPN resins were developed using an end-capping strategy. The curing behavior, processability, structure, and properties of the prepared resins were carefully studied and discussed. The end-capping reagent UPN expanded the processing temperature window of the prepolymers by reducing the melting temperature and delaying gelation. The end-capping adjusted resins exhibited a softer stiffness in the rubber state compared to the BPN resin, and they possessed shape memory properties with a glass transition temperature of around 300 °C. These SMPN resins exhibited a shape fixity rate of about 98 % and a shape recovery rate of around 97 %. Furthermore, the SMPN resins maintained excellent thermal stability, with a thermal decomposition temperature exceeding 445 °C and a carbon residue yield at 1000 °C exceeding 60 %. Ablation testing using an oxyacetylene flame demonstrated that SMPN exhibited outstanding ultrahigh-temperature resistance with a LAR less than 0.1 mm/s and a MAR lower than 0.1 g/s. Additionally, the annealing process of SMPN resulted in rigidification at high temperatures. Graphitization during the annealing process endowed the resin with conductivity, and the annealed SMPN even exhibited the ability to absorb electromagnetic waves, presenting new opportunities for diverse applications. This work not only advances the research of PN resins, but also enriches shape memory polymers with high deformation temperature and high-temperature resistance, expanding their potential applications in the aerospace industry and beyond.

CRediT authorship contribution statement

Rongxiang Hu: Writing – original draft. **Fenghua Zhang:** Supervision, Funding acquisition. **Lan Luo:** Methodology. **Linlin Wang:** Resources. **Yanju Liu:** Funding acquisition. **Jinsong Leng:** Funding acquisition.

Declaration of competing interest

The authors declare that they have no known competing financial interests or personal relationships that could have appeared to influence the work reported in this paper.

Data availability

Data will be made available on request.

Acknowledgements

This work was financially supported by the National Natural Science Foundation of China (Grant No. 92271112 and 92271206) and the National Key R&D Program of China (2022YFB3805700).

Appendix A. Supplementary data

Supplementary data to this article can be found online at https://doi.org/10.1016/j.cej.2024.150956.

References

[1] Y. Xia, Y. He, F. Zhang, Y. Liu, J. Leng, A review of shape memory Polymers and composites: mechanisms, materials, and applications, Adv. Mater. 33 (6) (2021), https://doi.org/10.1002/adma.202000713.
[2] T. Dayyoub, A.V. Maksimkin, O.V. Filippova, V.V. Tcherdyntsev, D.V. Telyshev, Shape memory Polymers as Smart materials, A Review, Polymers 14 (17) (2022), https://doi.org/10.3390/polym14173511.
[3] S. Yan, F. Zhang, L. Luo, L. Wang, Y. Liu, J. Leng, Shape memory Polymer composites: 4D printing, Smart structures, and applications, Research 6 (2023), https://doi.org/10.34133/research.0234.
[4] F. Zhang, N. Wen, L. Wang, Y. Bai, J. Leng, Design of 4D printed shape-changing tracheal stent and remote controlling actuation, Int. J. Smart Nano Mater. 12 (4) (2021) 375–389, https://doi.org/10.1080/19475411.2021.1974972.
[5] Q. Ze, X. Kuang, S. Wu, J. Wong, S.M. Montgomery, R. Zhang, J.M. Kovitz, F. Yang, H.J. Qi, R. Zhao, Magnetic shape memory Polymers with integrated multifunctional shape manipulation, Adv. Mater. 32 (4) (2020), https://doi.org/10.1002/adma.201906657.
[6] N. Li, W. Zhao, F. Li, L. Liu, Y. Liu, J. Leng, A 4D-printed programmable soft network with fractal design and adjustable hydrophobic performance, Matter 6 (3) (2023) 940–962, https://doi.org/10.1016/j.matt.2022.12.010.
[7] L. Luo, F. Zhang, L. Wang, Y. Liu, J. Leng, Recent advances in shape memory Polymers: multifunctional materials, multiscale structures, and applications, Adv. Funct. Mater. (2023), https://doi.org/10.1002/adfm.202312036.
[8] L. Luo, F. Zhang, L. Wang, Y. Liu, J. Leng, Multidimensional cross-linked network strategies for rapidly, reconfigurable, refoldable shape memory polymer, Chem. Eng. J. 478 (2023), https://doi.org/10.1016/j.cej.2023.147428.
[9] Y. Shi, H. Chen, X. Guan, High shape memory properties and high strength of shape memory polyurethane nanofiber-based yarn and coil, Polym. Test. 101 (2021), https://doi.org/10.1016/j.polymertesting.2021.107277.
[10] W. Liu, A. Wang, R. Yang, H. Wu, S. Shao, J. Chen, Y. Ma, Z. Li, Y. Wang, X. He, J. Li, H. Tan, Q. Fu, Water-triggered stiffening of shape-memory polyurethanes composed of Hard backbone dangling PEG soft segments, Adv. Mater. 34 (46) (2022), https://doi.org/10.1002/adma.202201914.
[11] M.J. Jo, H. Choi, H. Jang, W.-R. Yu, M. Park, Y. Kim, J.K. Park, J.H. Youk, Preparation of epoxy-based shape memory polymers for deployable space structures using diglycidyl ether of ethoxylated bisphenol-a, J. Polym. Res. 26 (6) (2019), https://doi.org/10.1007/s10965-019-1801-x.
[12] L. Luo, F. Zhang, W. Pan, Y. Yao, Y. Liu, J. Leng, Shape memory polymer foam: active deformation, simulation and validation of space environment, Smart Mater. Struct. 31 (3) (2022), https://doi.org/10.1088/1361-665X/ac4ba8.
[13] F. Xie, L. Huang, Y. Liu, J. Leng, Synthesis and characterization of high temperature cyanate-based shape memory polymers with functional polybutadiene/acrylonitrile, Polymer 55 (23) (2014) 5873–5879, https://doi.org/10.1016/j.polymer.2014.07.035.
[14] L. Wang, F. Zhang, Y. Liu, S. Du, J. Leng, Thermal, mechanical and shape fixity behaviors of shape memory cyanate under gamma-ray radiation, Smart Mater. Struct. 31 (4) (2022), https://doi.org/10.1088/1361-665X/ac5538.
[15] S. Basak, A. Bandyopadhyay, Solvent Responsive Shape Memory Polymers-Evolution, Current Status, and Future Outlook, Macromolecular Chemistry and Physics 222(19) (2021). https://doi.org/10.1002/macp.202100195.
[16] W. Tan, J. Lv, R. Li, J. Hu, K. Zeng, G. Yang, Bio-based adenine-containing copolyimides with high switching temperatures and high-strain storage, Mol. Syst. Des. Eng. 7 (8) (2022) 986–995, https://doi.org/10.1039/d2me00031h.
[17] Z. Zhao, Y. Gu, D. Chao, X. Liu, Synthesis and properties of shape memory poly (aryl ether ketone)s, Eur. Polym. J. 116 (2019) 336–341, https://doi.org/10.1016/j.eurpolymj.2019.04.026.
[18] T.M. Keller, D.D. Dominguez, High temperature resorcinol-based phthalonitrile polymer, Polymer 46 (13) (2005) 4614–4618, https://doi.org/10.1016/j.polymer.2005.03.068.
[19] F. Zhao, R. Liu, X. Yu, K. Naito, X. Qu, Q. Zhang, A high temperature polymer of phthalonitrile-substituted phosphazene with low melting point and good thermal stability, J. Appl. Polym. Sci. 132 (39) (2015), https://doi.org/10.1002/app.42606.
[20] G. Wang, Y. Guo, Y. Han, Z. Li, J. Ding, H. Jiang, H. Zhou, T. Zhao, Enhanced properties of phthalonitrile resins reinforced by novel phthalonitrile-terminated polyaryl ether nitrile containing fluorene group, High Perform. Polym. 32 (1) (2020) 3–11, https://doi.org/10.1177/0954008319847259.
[21] S. Liu, L. Tu, C. Liu, L. Tong, Z. Bai, G. Lin, K. Jia, X. Liu, Interfacial crosslinking enabled super-engineering polymer-based composites with ultra-stable dielectric properties beyond 350 degrees C, J. Alloy. Compd. 891 (2022), https://doi.org/10.1016/j.jallcom.2021.161952.
[22] H. Gu, C. Gao, A. Du, Y. Guo, H. Zhou, T. Zhao, N. Naik, Z. Guo, An overview of high-performance phthalonitrile resins: fabrication and electronic applications, J. Mater. Chem. C 10 (8) (2022) 2925–2937, https://doi.org/10.1039/d1tc05715d.
[23] D. Zhang, X. Liu, X. Bai, Y. Zhang, G. Wang, Y. Zhao, X. Li, J. Zhu, L. Rong, C. Mi, Synthesis, characterization and properties of phthalonitrile-etherified resole resin, E-Polymers 20 (1) (2020) 500–509, https://doi.org/10.1515/epoly-2020-0051.
[24] C. Gao, M. Yang, W. Xie, H. Zhang, H. Gu, A. Du, Z. Shi, Y. Guo, H. Zhou, Z. Guo, Adjustable magnetoresistance in semiconducting carbonized phthalonitrile resin, Chem. Commun. 57 (77) (2021) 9894–9897, https://doi.org/10.1039/d1cc04300e.
[25] C. Liu, B. Zhang, M. Sun, X. Liu, X. Zhang, J. Li, L. Wang, H. Zhou, Novel low-melting bisphthalonitrile monomers: synthesis and their excellent adhesive performance, Eur. Polym. J. 153 (2021), https://doi.org/10.1016/j.eurpolymj.2021.110511.
[26] W. Kong, J. Sun, M. Gao, T. Li, M. Liu, Y. Song, High-performance boron-containing phthalonitrile resins, Polym. Chem. 14 (19) (2023) 2317–2325, https://doi.org/10.1039/d3py00070b.
[27] Z. Zhang, Z. Li, H. Zhou, X. Lin, T. Zhao, M. Zhang, C. Xu, Self-catalyzed silicon-containing phthalonitrile resins with low melting point, excellent solubility and thermal stability, J. Appl. Polym. Sci. 131 (20) (2014), https://doi.org/10.1002/app.40919.
[28] X. Peng, H. Sheng, H. Guo, K. Naito, X. Yu, H. Ding, X. Qu, Q. Zhang, Synthesis and properties of a novel high-temperature diphenyl sulfone-based phthalonitrile

polymer, High Perform. Polym. 26 (7) (2014) 837–845, https://doi.org/10.1177/0954008314532479.
[29] Z. Chen, L. Wang, J. Lin, L. Du, A theoretical insight into the curing mechanism of phthalonitrile resins promoted by aromatic amines, PCCP 23 (32) (2021) 17300–17309, https://doi.org/10.1039/d1cp01947c.
[30] M. Laskoski, D.D. Dominguez, T.M. Keller, Synthesis and properties of a bisphenol a based phthalonitrile resin, J. Polym. Sci. Part A Polym. Chem. 43 (18) (2005) 4136–4143, https://doi.org/10.1002/pola.20901.
[31] T. Liu, Y. Yang, T. Wang, H. Wang, H. Zhang, Y. Su, Z. Jiang, Synthesis and properties of poly(aryl ether ketone)-based phthalonitrile resins, Polym. Eng. Sci. 54 (7) (2013) 1695–1703, https://doi.org/10.1002/pen.23709.
[32] S. Liao, H. Wu, X. He, J.-H. Hu, R. Li, Y. Liu, J. Lv, Y. Liu, Z. Liu, K. Zeng, G. Yang, Promoting effect of methyne/methylene moiety of bisphenol E/F on phthalonitrile resin curing: expanding the structural design route of phthalonitrile resin, Polymer 210 (2020), https://doi.org/10.1016/j.polymer.2020.123001.
[33] C. Gao, H. Gu, A. Du, H. Zhou, D. Pan, N. Naik, Z. Guo, Polyaniline facilitated curing of phthalonitrile resin with enhanced processibility and mechanical property, Polymer 219 (2021), https://doi.org/10.1016/j.polymer.2021.123533.
[34] T.R. Walton, J.R. Griffith, J.P. Reardon, Electrically conducting polymers from conjugated bis-phthalonitrile monomers, J. Appl. Polym. Sci. 30 (7) (1985) 2921–2939, https://doi.org/10.1002/app.1985.070300717.
[35] D.B. Schuepfer, F. Badaczewski, J.M. Guerra-Castro, D.M. Hofmann, C. Heiliger, B. Smarsly, P.J. Klar, Assessing the structural properties of graphitic and non-graphitic carbons by raman spectroscopy, Carbon 161 (2020) 359–372, https://doi.org/10.1016/j.carbon.2019.12.094.
[36] M.A. Pimenta, G. Dresselhaus, M.S. Dresselhaus, L.G. Cançado, A. Jorio, R. Saito, Studying disorder in graphite-based systems by raman spectroscopy, PCCP 9 (11) (2007) 1276–1290, https://doi.org/10.1039/b613962k.
[37] Z.-L. Wang, K. Zheng, J.-Y. Xiong, L.-J. Xun, Y. Han, Y. Guo, L. Ye, W.-J. Han, J. Wang, W.-B. Liu, H. Zhou, T. Zhao, Ceramic precursor-phthalonitrile hybrid with improved high heat resistance through constructing binary continuous phases, Composites, Part A 162 (2022), https://doi.org/10.1016/j.compositesa.2022.107123.
[38] X. Xing, Y. Zhao, X. Zhang, J. Wang, T. Hong, Y. Li, S. Wang, C. Zhang, X. Jing, Healable ablative composites from synergistically crosslinked phenolic resin, Chem. Eng. J. 447 (2022), https://doi.org/10.1016/j.cej.2022.137571.
[39] S. Zhao, L. Pei, J. He, X. Zhang, W. Hu, H. Yan, G. Zhao, C. Zhang, Z. Wang, Curing mechanism, thermal and ablative properties of hexa-(4-amino-phenoxy) cyclotriphosphazene/benzoxazine blends, Composites, Part B 216 (2021), https://doi.org/10.1016/j.compositesb.2021.108838.
[40] S. Wang, L. Wang, H. Su, C. Li, W. Fan, X. Jing, Enhanced thermal resistance and ablation properties of ethylene-propylene-diene monomer rubber with boron-containing phenolic resins, React. Funct. Polym. 170 (2022), https://doi.org/10.1016/j.reactfunctpolym.2021.105136.
[41] X. Yan, H. Huang, Z. Fan, C. Hong, P. Hu, Assessment of a 3D ablation material response model for lightweight quartz fiber reinforced phenolic composite, Polym. Compos. 43 (11) (2022) 8341–8355, https://doi.org/10.1002/pc.27005.
[42] Z.-X. Zhou, Y. Li, J. Zhong, Z. Luo, C.-R. Gong, Y.-Q. Zheng, S. Peng, L.-M. Yu, L. Wu, Y. Xu, High-performance cyanate Ester resins with interpenetration networks for 3D printing, ACS Appl. Mater. Interfaces 12 (34) (2020) 38682–38689, https://doi.org/10.1021/acsami.0c10909.
[43] Y. Zi, D. Pei, J. Wang, S. Qi, G. Tian, D. Wu, High-temperature-induced shape memory copolyimide, Polymers 13 (19) (2021), https://doi.org/10.3390/polym13193222.
[44] S. Zhou, L. Yuan, G. Liang, A. Gu, Thermally resistant and strong shape memory bismaleimide resin with intrinsic halogen-free and phosphorus-free flame retardancy, J. Appl. Polym. Sci. 139 (47) (2022), https://doi.org/10.1002/app.53187.
[45] S. Yang, Y. He, J. Leng, Zwitterionic Poly(aryl ether ketone) with water-actuated reshaping-reconfiguration ability and triple shape memory effect, ACS Appl. Polym. Mater. 4 (6) (2022) 4286–4297, https://doi.org/10.1021/acsapm.2c00245.
[46] X.L. Wu, W.M. Huang, Z. Ding, H.X. Tan, W.G. Yang, K.Y. Sun, Characterization of the thermoresponsive shape-memory effect in poly(ether ether ketone) (PEEK), J. Appl. Polym. Sci. 131 (3) (2014) n/a-n/a, https://doi.org/10.1002/app.39844.
[47] X. Wang, Y. He, J. Leng, Shape memory polyimides and composites with tunable chain stiffness and ultrahigh transition temperature range, Compos. A Appl. Sci. Manuf. 163 (2022), https://doi.org/10.1016/j.compositesa.2022.107237.
[48] Y. Shi, R.A. Weiss, Sulfonated poly(ether ether ketone) Ionomers and their high temperature shape memory behavior, Macromolecules 47 (5) (2014) 1732–1740, https://doi.org/10.1021/ma500119k.
[49] Y. Gu, C. Ru, Z. Zhao, D. Chao, X. Liu, Performance enhancement of shape memory poly(aryl ether ketone) via photodimerization of pendant anthracene units, Eur. Polym. J. 123 (2020), https://doi.org/10.1016/j.eurpolymj.2019.109413.
[50] H. Gao, X. Lan, L. Liu, X. Xiao, Y. Liu, J. Leng, Study on performances of colorless and transparent shape memory polyimide film in space thermal cycling, atomic oxygen and ultraviolet irradiation environments, Smart Mater. Struct. 26 (9) (2017), https://doi.org/10.1088/1361-665X/aa7bd7.
[51] F. Wu, P. Hu, F. Hu, Z. Tian, J. Tang, P. Zhang, L. Pan, M.W. Barsoum, L. Cai, Z. Sun, Multifunctional MXene/C aerogels for enhanced microwave absorption and thermal insulation, Nano-Micro Letters 15 (1) (2023), https://doi.org/10.1007/s40820-023-01158-7.
[52] Z. Huang, R. Qin, H. Zhang, M. Guo, D. Zhang, C. Gao, F. Gao, X. Chen, M. Terrones, Y. Wang, Ambient-drying to construct unidirectional cellulose nanofibers/ carbon nanotubes aerogel with ultra-lightweight, robust, and superior microwave absorption performance, Carbon 212 (2023), https://doi.org/10.1016/j.carbon.2023.118150.
[53] G. Chen, H. Liang, J. Yun, L. Zhang, H. Wu, J. Wang, Ultrasonic field induces better crystallinity and abundant defects at grain Boundaries to develop CuS electromagnetic wave absorber, Adv. Mater. (2023), https://doi.org/10.1002/adma.202305586.